

Supporting Information for
“The 12 September 2016 M_L 5.8 mid-crustal earthquake in the Korean Peninsula and its seismic implications”

Tae-Kyung Hong^{1,*}, Junhyung Lee¹, Woohan Kim², In-Kyeong Hahm³, Nam Chil Woo¹, and Seongjun Park¹

¹Yonsei University, Department of Earth System Sciences, 50 Yonsei-ro, Seodaemun-gu Seoul 120-749, South Korea.

²Gyeongsang National University, Department of Earth and Environmental Sciences and RINS, Jinju, Gyeongsangnam-do 660-701, South Korea

³Korea Meteorological Administration, 61 16-Gil Yeouidaeband-ro Dongjak-gu Seoul 07062, South Korea

Contents of this file

1. Analysis
2. References
3. Figures S1 to S11

Introduction

This supporting information provides additional materials for analysis with references and figures.

Analysis

Strong high frequency seismic energy is radiated from the source, lasting in local distances (Fig. S1). The high frequency energy decays fast with distance. Seismic records in epicentral distance of 8.2 km (station USN) display stronger ground motions than those in epicentral distance of 5.8 km (station MKL). The observation suggests that site effects affect ground motions strongly.

Corresponding author: Tae-Kyung Hong, tkhong@yonsei.ac.kr

The horizontal displacement spectra at 3 stations in short distances are compared (Fig. S2(a),(b)). We observe characteristic high-frequency contents in the displacement spectra. The horizontal displacement spectra at station USN are compared with theoretical models (Fig. S2(c),(d)). Here the theoretical displacement spectrum model, Ω , is presented by [Brune, 1970]

$$\Omega(\omega) = \frac{M_0}{1 + (\omega/\omega_0)^2}, \quad (1)$$

where M_0 is the seismic moment, ω is the frequency, and ω_0 is the corner frequency. Here, an empirical relationship between the seismic moment and corner frequency is given by [Xie, 2002; Hong, 2010]

$$\log(\omega_0) = 4.603 - 0.308 \log(M_0). \quad (2)$$

The corner frequency (ω_0) for the M_L 5.8 earthquake is determined to be 0.39 Hz.

Theoretical displacement spectra with arbitrary seismic moments are presented in Fig. S2(c) and (d). The theoretical displacement spectra decay as ω^2 in high frequencies. On the other hand, the observed displacement spectra display decay rates of $\omega^{-1.19(\pm 0.02)}$ in the frequency range of 1-15 Hz. The high-frequency energy content suggests that the fault plane may be fresh or ruptured with a long recurrence time.

The focal depths of the mainshock and aftershocks range between 11 and 16 km (Fig. S3). Most events are distributed at depths between 13 and 15 km. We found the b value of the Gutenberg-Richter magnitude-frequency relationship for aftershocks to be 1.04 (Fig. S4). The minimum magnitude (M_{\min}) that ensures the completeness of the aftershock catalog is 1.6.

We apply VELHYPO for hypocentral parameter inversion of earthquakes [Kim *et al.*, 2014, 2016]. The hypocentral parameter inversion method yields an optimum velocity model for every event data set (Fig. S5). The inverted optimum velocity models are consistent among different data set. The mean velocity model generally agrees with a regional velocity model of Chang and Baag [2006] at depths greater than 3 km. On the other hand, the mean velocity model displays higher seismic velocities than an average global velocity model [ak135, Kennett *et al.*, 1995].

Once the hypocentral parameters and optimum velocity models are determined, we calculate the station correction terms from traveltimes residuals (Fig. S6). Positive station

correction values mean lower seismic velocities, and negative station correction values suggest higher seismic velocities. We find lateral perturbation in seismic velocities.

We determine the focal mechanism solutions of moderate-size earthquakes using a long-period waveform inversion [Dreger and Helmberger, 1990; Hong *et al.*, 2015]. The focal mechanism solutions of three largest earthquakes are presented (Figs. S7, S8, S8). The inverted focal mechanism solutions are consistent each other, agreeing with the fault geometry illuminated from spatial aftershock distribution.

Most aftershocks occurred around the fault where the Coulomb stresses decreased and large dynamic stress changes were produced (Fig. S10). On the other hand, the remote aftershocks are scattered in regions of elevated Coulomb stresses (Fig. S10). The aftershocks were induced by static and dynamic stress changes. Fig. S11 presents the dynamic stress induced by seismic waves from the M_L 5.8 earthquake. The induced peak dynamic stresses reach 11.5 bar in E-W direction, 7.6 bar in N-S direction, 3.7 in vertical direction, and 14.2 bar in the polarization direction.

References

- Brune, J. (1970), Tectonic stress and the spectra of seismic shear waves from earthquakes, *Journal of Geophysical Research*, *75*, 4997-5009.
- Chang, S.-J., and Baag, C.-E. (2006), Crustal structure in Southern Korea from joint analysis of regional broadband waveforms and travel times, *Bulletin of the Seismological Society of America*, *96*, 856-870.
- Dreger, D.S., and Helmberger, D.V. (1990), Broadband modeling of local earthquakes, *Bulletin of the Seismological Society of America*, *80*, 1162-1179.
- Hong, T.-K. (2010), Lg attenuation in a region with both continental and oceanic environments, *Bulletin of the Seismological Society of America*, *100* (2), 851-858.
- Hong, T. K., Lee, J., and Hough, S. E. (2015), Long-term evolution of intraplate seismicity in stress shadows after a megathrust, *Physics of the Earth and Planetary Interiors*, *245*, 59-70.
- Kennett, B. L. N., Engdahl, E. R., and Buland, R. (1995), Constraints on seismic velocities in the Earth from traveltimes, *Geophysical Journal International*, *122*, 108-124.
- Kim, W., Hong, T.-K., and Kang, T.-S. (2014), Hypocentral parameter inversion for regions with poorly known velocity structures, *Tectonophysics*, *627*, 182-192.

Kim, W., Hong, T. K., Lee, J., and Taira, T. A. (2016), Seismicity and fault geometry of the San Andreas fault around Parkfield, California and their implications, *Tectonophysics*, 677, 34-44.

Xie, J. (2002), Source scaling of Pn and Lg spectra and their ratios from explosions in central Asia: Implications for the identification of small seismic events at regional distances, *Journal of Geophysical Research*, 107 (B7), 2128, doi 10.1029/2001JB000509.

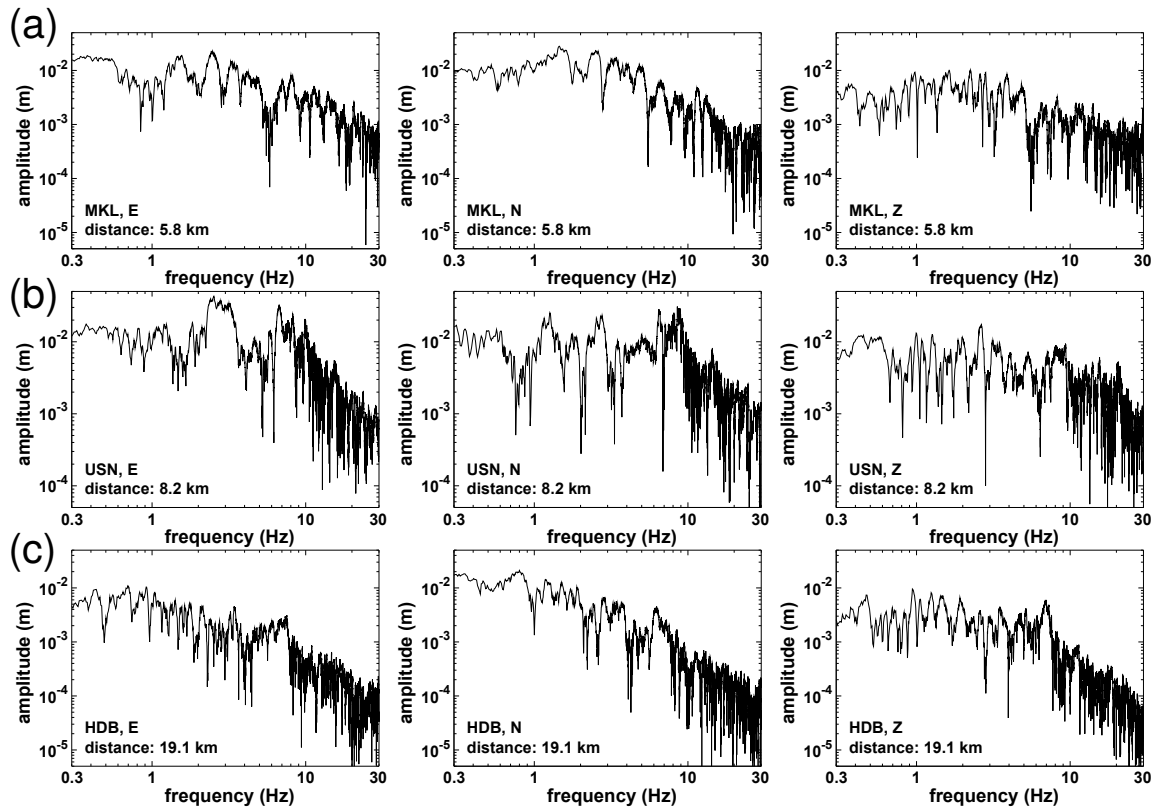


Figure S1. Spectral amplitudes of velocity ground motions in E-W, N-S, and vertical components at stations (a) MKL, (b) USN, and (c) HDB. Strong high-frequency energy develops in local distances.

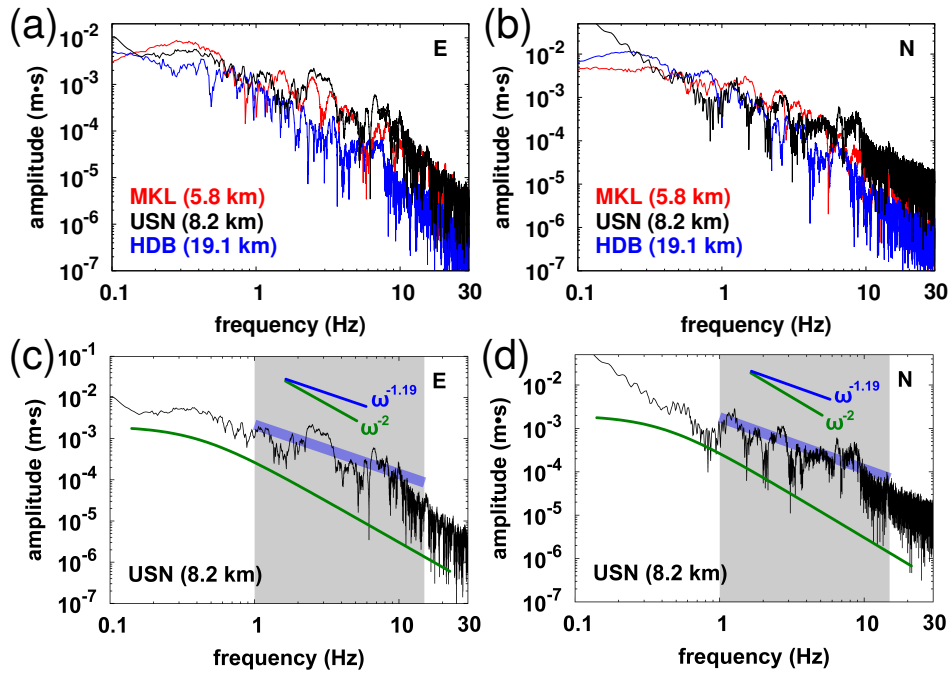


Figure S2. Horizontal displacement spectra at 3 stations (MKL, USN, HDB) in short distances: (a) E-W components and (b) N-S components. Characteristic high-frequency contents are observed. The observed displacement spectra at station USN are compared with the theoretical models with arbitrary seismic moments. The horizontal displacement spectra decay as $\omega^{-1.19(\pm 0.02)}$ in the frequency (ω) range of 1-15 Hz where ω is the frequency.

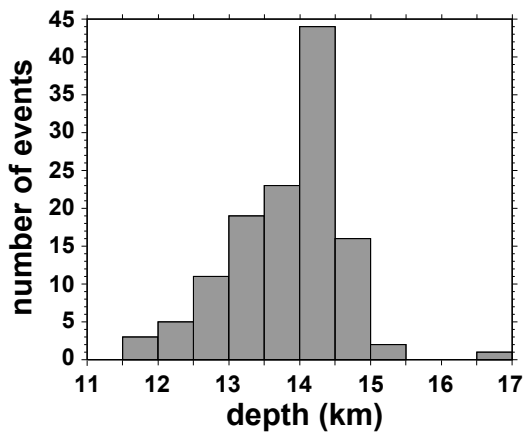


Figure S3. Focal-depth distribution of earthquakes. Most events are distributed at depths between 13 and 15 km.

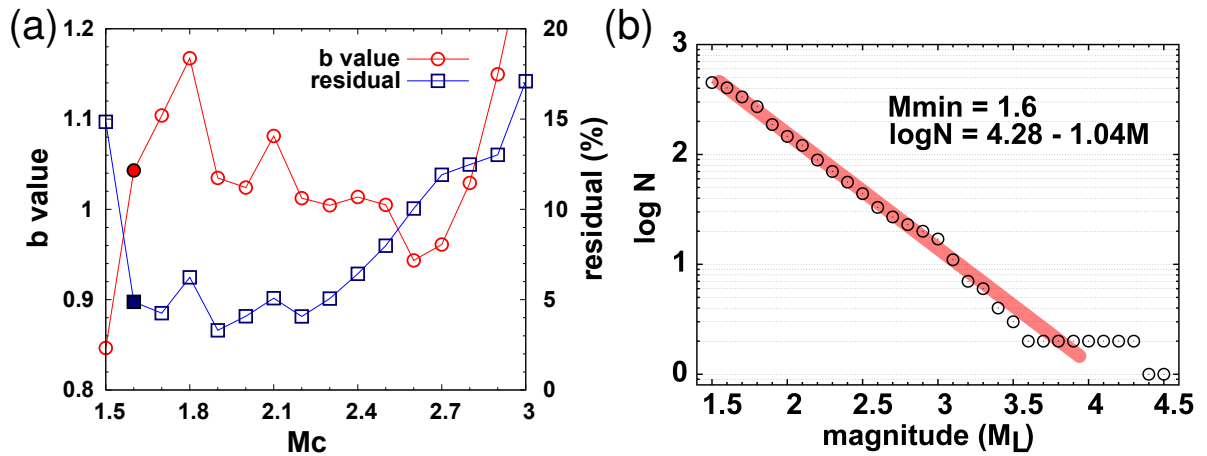


Figure S4. (a) Variation of residuals as a function of cutoff magnitude (M_c) in determination of the Gutenberg-Richter magnitude-frequency relationship. The residuals are less than 6 % in a range of $1.6 \leq M_c \leq 2.3$. (b) The Gutenberg-Richter magnitude-frequency relationship for the aftershocks with the minimum magnitude of $M_{\min} = 1.6$. The b value is determined to be 1.04.

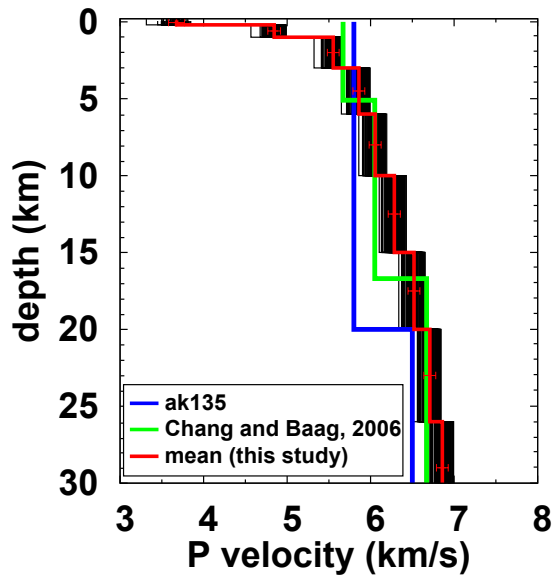


Figure S5. Optimum P velocity models (black lines) derived from the hypocentral parameter inversion of earthquakes. The mean velocity model is presented with a red solid line. An average global 1-D velocity model [ak135, Kennett *et al.*, 1995] and a regional 1-D velocity model [Chang and Baag, 2006] are presented for comparison.

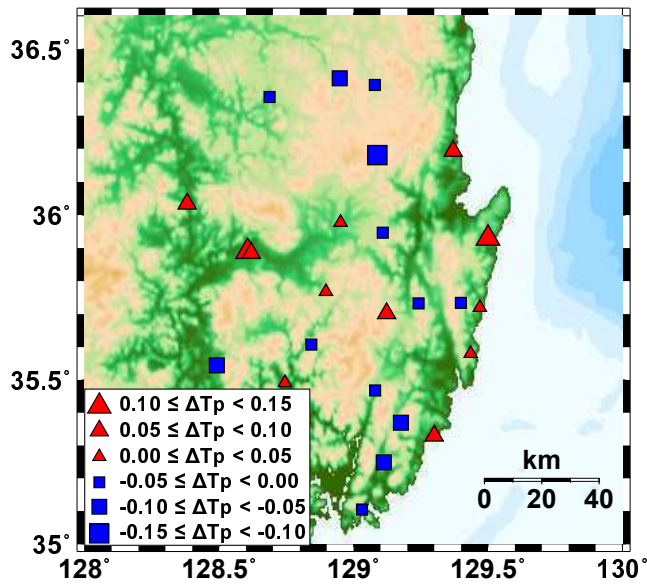


Figure S6. Station correction terms for P travel times (ΔT_p) determined from the hypocentral parameter inversions, presenting lateral seismic velocity perturbations.

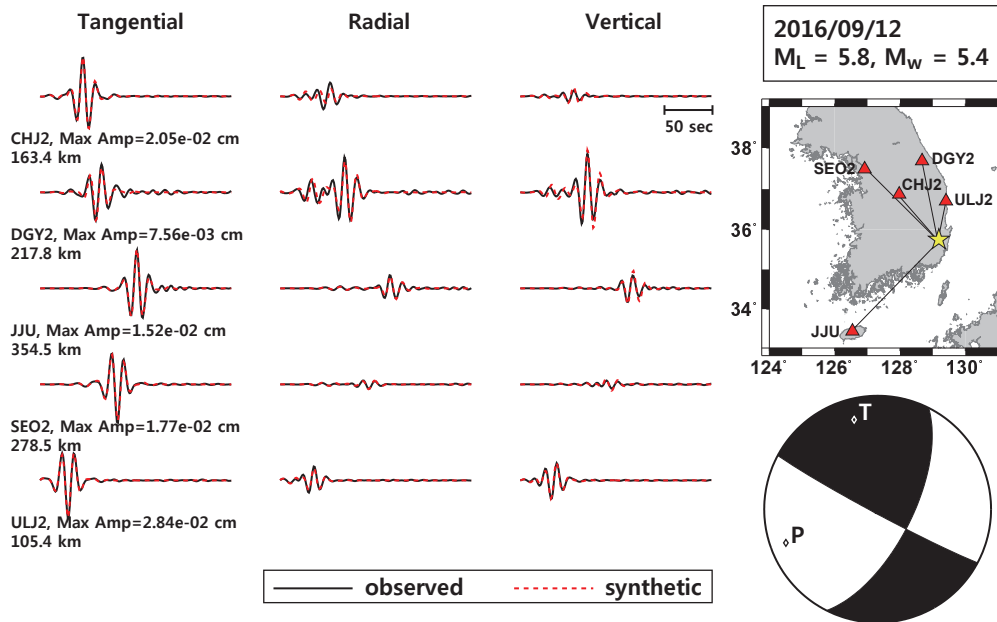


Figure S7. A Long-period waveform inversion for the 12 September 2016 M_L 5.8 earthquake.

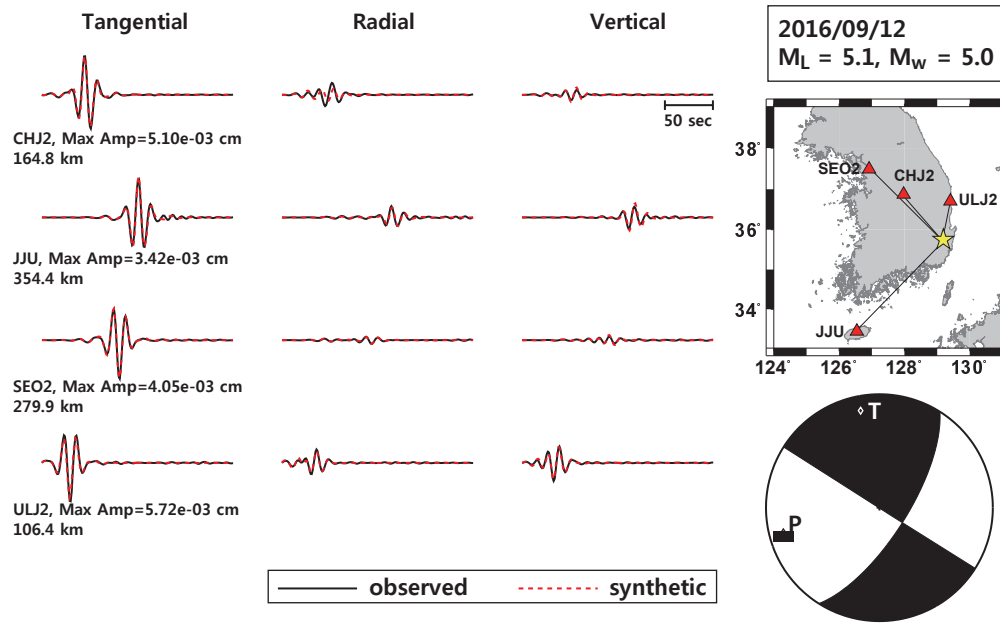


Figure S8. A Long-period waveform inversion for the 12 September 2016 M_L 5.1 earthquake.

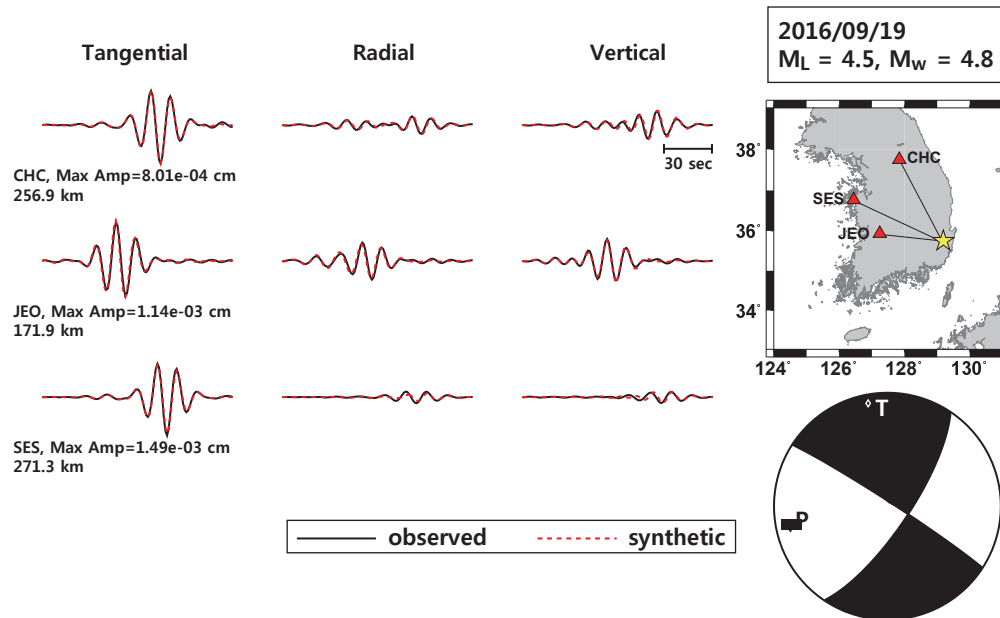


Figure S9. A Long-period waveform inversion for the 19 September 2016 M_L 4.5 earthquake.

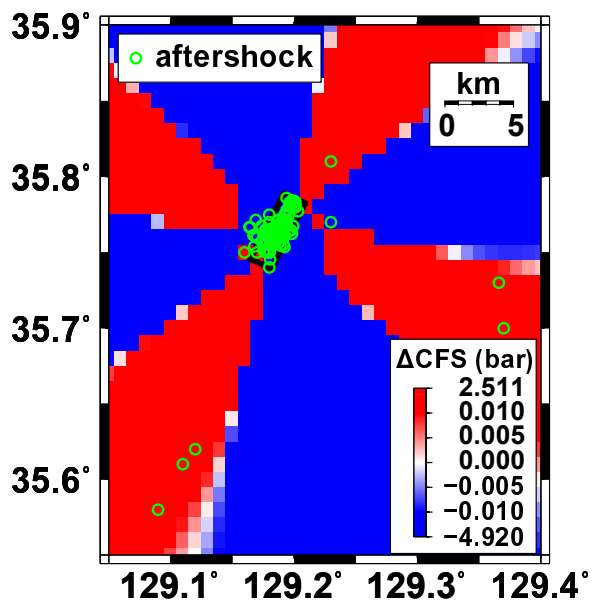


Figure S10. Spatial distribution of aftershocks and Coulomb stress changes. The fault dimension is marked with thick solid lines. Most aftershocks occurred on the fault. Remote earthquakes occurred in the regions of elevated Coulomb stresses.

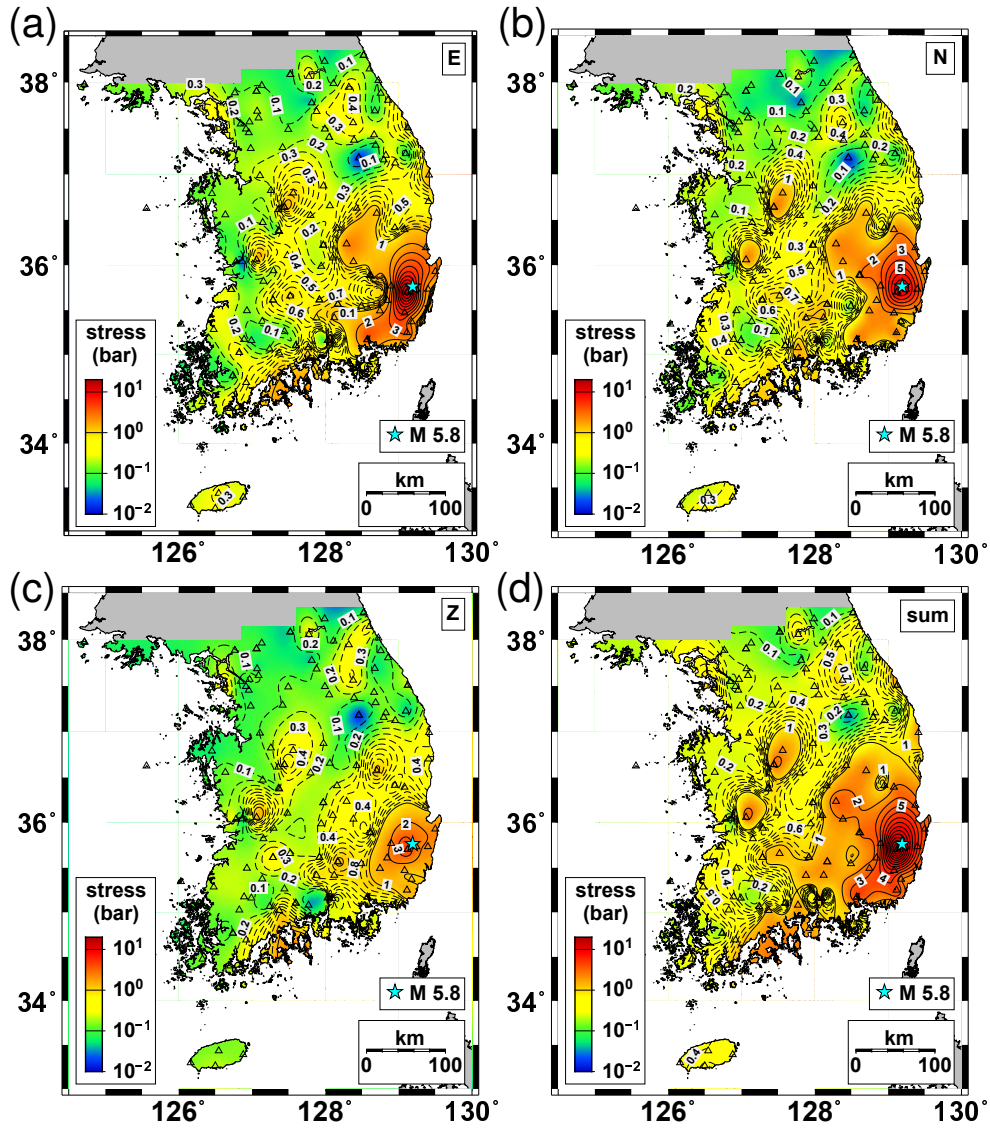


Figure S11. Peak dynamic stresses induced by seismic waves from the $M_L 5.8$ earthquake: (a) E-W component, (b) N-S component, (c) vertical component, and (d) vector sum.